

Extended and adjustable field-of-view of variable interscan time analysis by ammonite-scanning swept-source optical coherence tomography angiography

TOSHIHIRO MINO,^{1,2} YOSHIKIYO MORIGUCHI,^{2,*}  MASATO TAMURA,² AKIKO MATSUMOTO,²  ATSUSHI KUBOTA,² MASAHIRO AKIBA,²  YUNCHAN HWANG,³ SHUICHI MAKITA,⁴  YOSHIAKI YASUNO,⁴  HIROSHI ENAIDA,⁵ JAMES G. FUJIMOTO,³ AND ZHENGUO WANG¹ 

¹Topcon Advanced Biomedical Imaging Laboratory, Topcon Medical Systems, 111 Bauer Drive, Oakland, NJ 07436, USA

²Research & Development Division, Topcon Corporation, 75-1 Hasunuma-cho, Itabashi-ku, Tokyo 174-8580, Japan

³Department of Electrical Engineering and Computer Science, Research Laboratory of Electronics, Massachusetts Institute of Technology, Cambridge, MA 02139, USA

⁴Computational Optics Group, University of Tsukuba, 1-1-1 Tennodai, Tsukuba, Ibaraki 305-8573, Japan

⁵Department of Ophthalmology, Faculty of Medicine, Saga University, 5-1-1 Nabeshima, Saga 849-8501, Japan

*ymoriguchi@topcon.com

Abstract: A novel scanning protocol, ammonite scan, is proposed for widefield optical coherence tomography angiography (OCTA) and relative retinal blood flow velocity imaging in the human retina using variable interscan time analysis (VISTA). A repeated circle scan using a 400 kHz swept-source was employed to achieve an interscan time of 1.28 ms. The center of the repeated circular scan continuously moved spirally towards the peripheral region, ensuring an extended and adjustable scan range while preserving the short interscan time. Image artifacts due to eye movement were eliminated via extra motion-correction processing using data redundancy. The relative blood flow velocity in superficial and deep plexus layers was calculated from the VISTA image, and their ratio was used to explore the microvascular flow parameter in the healthy human eye.

© 2023 Optica Publishing Group under the terms of the [Optica Open Access Publishing Agreement](#)

1. Introduction

The retina is one of the highest metabolic demanding neural tissues in the human body and requires a blood supply commensurate with its consumption of nutrients, such as oxygen and glucose, to effectively maintain cell survival and function. The retinal blood supply is actively regulated in the intricate and heterogeneous retinal microvascular network [1,2]. Early detection of retinal vasculature dysfunction may help prevent irreversible damage to retinal neurons.

Optical coherence tomography angiography (OCTA) is a non-invasive method for assessing perfusion in the retinal vasculature [3–5]. Recent advancements in OCTA-scan rates have led to the development of advanced OCTA techniques, such as variable interscan time analysis (VISTA) [6]. In other words, high-speed OCT with VISTA can characterize not only the morphology of retinal vasculature but also blood flow dynamics within retinal vasculature. In the original VISTA algorithm, the relative blood flow speed was calculated based on the ratio of OCTA at two different interscan times, that is, the time interval between sequentially acquired B-scans. By employing VISTA, some pioneering studies have successfully revealed relative retinal blood flow

speed impairment in patients with age-related macular degeneration, diabetic retinopathy (DR), and polypoidal choroidal vasculopathy [6–12]. Silva *et al.* did studies showing the usefulness of widefield retinal imaging on DR classification [13], and Zhang *et al.* demonstrated the potential of widefield OCTA [14]. Besides, recent clinical studies have shown that the vascular lesions are more prominently distributed in the peripheral retina [15]. Thus, there could be potential merits to studying retinal blood flow speeds not only in the fovea but also at a larger field of view (FOV).

The requirement for a short interscan time limits the FOV of VISTA imaging. The previous studies on VISTA referenced above suggest that interscan time shorter than 1.5 ms is an appropriate temporal resolution to extract faint changes in the OCT signal derived from human retinal capillary flow. When using raster scans with such a short interscan time, the practically achievable FOV is small, such as 3×3 mm, because of the limited response time of Galvanometer scanners (GSs), its fly-back motion in every B-scan and limited A-line rate of OCT system.

As an alternative to conventional raster scans [16], various beam steering protocols have been proposed, including nonlinear scans [17], bidirectional scans [18,19], spiral scans [20,21], and cycloid scans [22]. Chen *et al.* and Makita *et al.* used a Lissajous scan to reduce the image artifacts of involuntary eye movements during OCT measurement [23–25]. Recently, the same group extended the FOV of OCTA with the Lissajous scan via the addition of slow circular drift to the center of the Lissajous scan; this is referred to as the convolutional Lissajous scan method [26]. This type of scan is suitable for expanding the FOV of VISTA because of the decoupling of FOV from the interscan time. The cycloid scan can also be used to achieve a wide FOV [22]. Cycloid scanning uses a fast and precise circular scan over a smaller FOV, combined with a slower translational scan, which moves the circle to generate a spiral scan. OCTA and OCT of the gastrointestinal tract have been demonstrated using a cycloid scanning tethered capsule with a piezoelectric scanner for high-speed circular scanning suitable for OCTA coupled to a micrometer actuated reflector, which translates the circular scan around the capsule circumference to achieve a wide FOV.

In this study, a novel scanning protocol was devised following the strategy of the convolutional Lissajous scan and a cycloid scan, wherein the fast and slow scans were circle and spiral scans, respectively. The circle scan is repeated while the center of the circle is moved to the periphery in a spiral manner to cover a larger FOV. Hereafter, the scan pattern is referred to as an “ammonite scan” because the trajectory of the circle resembles the appearance of the ammonite fossil. The circle B-scan maximizes the scanning speed by driving a two-axis GS simultaneously with no flyback motion and enables to achieve the sufficiently shorter interscan time required for VISTA. In addition, the circle scan has a constant scanning velocity, which makes it easier to control the sampling density compared to that in the Lissajous scan. The spiral slow scan has a high affinity with the centrosymmetric optics of the measurement system and the eyeball, and the FOV is effectively extended as needed while maintaining a short interscan time. For motion correction, a previously developed motion correction algorithm [26], which is used in the Lissajous scan, can also be applied to the ammonite scan. Further, the redundancy of the captured dataset is utilized to apply the motion correction process, which effectively reduces motion artifacts without using additional eye-tracking features.

As a proof of concept, in this study, we performed widefield OCT/OCTA imaging using the ammonite scan method and applied VISTA to differentiate the relative blood flow velocity in the retinal microvascular network. The repeatability of the measurement was validated in subjects with normal human eyes.

2. Methods

2.1. System

We employed a SS-OCT prototype system (Topcon Corp., Tokyo, Japan) using a tunable vertical-cavity surface-emitting laser (VCSEL) light source with an A-scan rate of 400 kHz [27]. The

center wavelength of the light source was 1050 nm with a tuning range of approximately 100 nm, which is invisible to the human eye. Our system is based on the Mach-Zehnder type interferometer, wherein the collimated light is directed to the eye via a two-axis GS (model 6210 H; Cambridge Technology Inc., USA) with a 5-mm aperture size mirror placed near the pupil conjugate. The OCT interference signal was detected by a balanced receiver (PDB481C-AC, Thorlabs, Inc.), sampled by a 1.8 GSPS dual-channel A/D acquisition board. The OCT interference signal was then resampled using a simultaneously acquired Mach-Zehnder interferometer (MZI) signal and A-line trigger generated by the fiber Bragg grating. The resampled OCT signal was subjected to background subtraction, apodization, numerical dispersion correction, and zero-padding, before an inverse Fourier transformation from the frequency to the spatial domain. The incident beam diameter ($1/e^2$ width) was 1.3 mm at the pupil. The depth resolution and depth imaging range were approximately 8.0 μm (full-width-at-half-maximum) and 5.0 mm in the tissue, respectively. The incident power on the cornea was adjusted to 1.85 mW, which is within the ISO 15004-2:2007 and ANSI Z80-36:2016 standards for 1050 nm light.

2.2. OCTA and ammonite scanning protocol

The GSs were driven by the waveform described by the following equations:

$$x(i_f, j_s) = \frac{L_f}{2\pi} \cos \left\{ \frac{2\pi}{N_f} i_f + \varphi(j_s) \right\} + R(j_s) \cos(\varphi(j_s)) \quad (1)$$

$$y(i_f, j_s) = \frac{L_f}{2\pi} \sin \left\{ \frac{2\pi}{N_f} i_f + \varphi(j_s) \right\} + R(j_s) \sin(\varphi(j_s)) \quad (2)$$

$$j_s = \text{floor}(i_f / N_f) \quad (3)$$

where the floor(.) function is used to round down the values to the closest integer number. The parameters in the equations are defined as follows:

- i_f : i^{th} sampling index
- j_s : j^{th} slow scan index
- L_f : Fast (circular) scan length
- L_s : Slow (spiral) scan length
- L_Δ : Gap length between adjacent spiral scan trajectories
- N_f : Number of sampling points for the fast scan
- N_s : Number of sampling points for the slow scan

The scan pattern is referred to as an ammonite scan as mentioned earlier. The first term on the right side of Eqs. (1) and (2) represents the fundamental circle scan waveform, and the second term represents the spiral waveform. Further, $\varphi(j_s)$ and $R(j_s)$ represent the phase and radius of the spiral scanning position determined by j_s , respectively, and they are designed to ensure spiral scanning with a constant linear velocity. The $\varphi(j_s)$ was introduced to the phase of the circle scan waveform as well as to optimize the continuity and minimize the acceleration at the transitions between adjacent circle scans. To improve the sampling density and uniformity at the beginning of the spiral scan, a circular scan was employed at the first 270° (N_{circle} points) instead of the spiral scan. In the result, $\varphi(j_s)$ and $R(j_s)$ are described as

If $j_s < N_{circle}$

$$\varphi(j_s) = \frac{4L_s}{3L_\Delta N_{circle}} j_s, \quad R(j_s) = \frac{3L_\Delta}{4} \quad (4)$$

If $N_{circle} < i_c < N_s$

$$\varphi(j_s) = \sqrt{\frac{4\pi L_s j_s}{L_\Delta N_s} - \frac{9\pi^2 L_\Delta}{4}}, \quad R(j_s) = \frac{L_\Delta}{2\pi} \varphi(j_s) \quad (5)$$

Here,

$$N_{circle} = \frac{9\pi L_\Delta N_s}{8L_s} \quad (6)$$

In addition, to improve continuity from the j^{th} to $j + 1^{\text{th}}$ circle scan, N_t transition points were introduced, wherein no data acquisition was performed, and the stability of the individual circle B-scan was ensured; N_t was determined from j_s as follows:

$$N_t(j_s) = \text{floor} \left\{ (\varphi(j_s + 1) - \varphi(j_s)) \frac{N_f}{2\pi} + \frac{L_s}{N_s} \Delta \frac{N_f}{L_f} \right\} \quad (7)$$

In OCTA imaging, the circle B-scans were repeated at the same location several times, followed by the next location along a spiral trajectory via the transition points.

Figure 1 illustrates a scanning trajectory for $L_f = 4.5 \text{ mm}$, $L_s = 36 \text{ mm}$, $L_\Delta = 0.74 \text{ mm}$, $N_f = 512$, and $N_s = 2048$. These parameters enabled the capture of a 6-mm-diameter region with the ammonite scan comprising circular fast scans with a 1.4-mm diameter. For illustration, N_f and N_s were set to small numbers compared to the actual scans for better visualization of the scanning trajectory. L_Δ determines overlap between inner circle and outer circle. More overlap introduces redundancy of data sampling and can increase sampling density and robustness of motion correction process without data-missing area. In contrast, less overlap leads to faster imaging. We empirically set the overlap as 45% which can comfortably avoid data-missing area even when large eye motion occurs. In this parameter setting, the sampling density is not perfectly uniform over the entire area, where it is relatively low density in the outermost trajectory region. This scan pattern was designed for simplicity and image quality at the center of the scan area although a more uniform sampling density can be achieved across the scan area by introducing variable number of N_f , L_f , L_Δ , etc. The missing pixels in transforming to the Cartesian coordinate, described in the next section, was calculated to be 5% and 1% in most of the scanned area when the pixel bin size was set to $9 \times 9 \mu\text{m}^2$ and $12 \times 12 \mu\text{m}^2$, respectively. In our method, such missing pixels were calculated by interpolating neighboring pixels.

In addition, real-time blink detection and rescanning functions have been implemented to ensure the success rate of image reconstruction. Interference signals are Fourier-transformed at every 10 frames (13 ms) and a blink is detected when the maximum power of the spectrum is less than a threshold. If a blink is detected during the measurement, the scanner returns to the location where the previous fast scan was successful and then resumes the rest of the scan. Obvious blinks were eliminated as per the above rescan method. Further, the redundancy of the ammonite scan and motion compensation procedure described in Sec. 2.3 enabled the compensation for slight blinks and/or eye motion during scanning. Thus, the patient was allowed to blink during the measurement.

The total data acquisition time can be estimated from N_f , N_s , and the number of repetitions; it was approximately 2.6 s and 21 s when the scan pattern illustrated in Fig. 1 was used for structural OCT (single repetition) and VISTA (eight repetitions), respectively. Note that it can vary with the number of blinks detected. As indicated by the red line in Figs. 1(a) and (c), adjacent fast scans between the j^{th} and $j + 1^{\text{th}}$ circle scan were smoothly connected with the transition points along the tangential line of the circle. Further, the scanning duty ratio excluding the transition points was 99.4% for a single repetition, which increased with the number of repetitions, and reached 99.9% at eight repetitions.

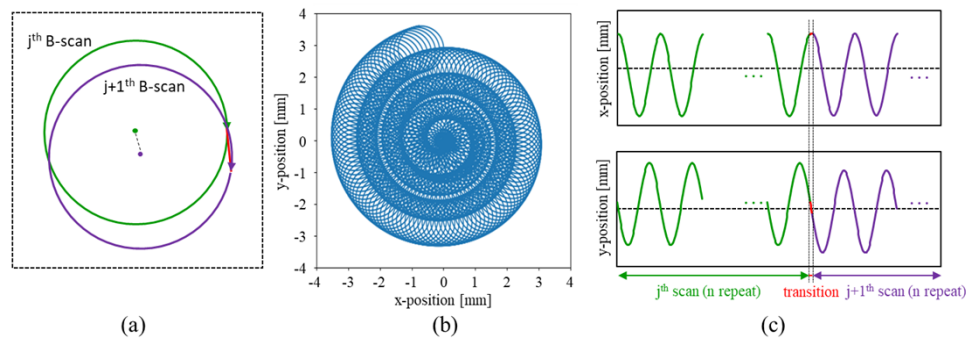


Fig. 1. (a) Fundamental fast circle B-scan at two different positions. OCTA imaging was repeated n times in each location, following which it was moved to the next $j + 1$ location. The transition points indicated by the red line was introduced between B-scans where no data acquisition was performed. (b) The trajectory of the widefield scan, named ammonite scan. (c) Waveforms applied to the two-axis GSs.

2.3. Image reconstruction

The 3D OCT/OCTA data captured by the ammonite scan were then reconstructed during post-processing, which was performed on a graphical processing unit (GPU: GeForce RTX 3090, Nvidia Corp., CA, USA). Most reconstruction workflows are consistent with the previously reported 3D strip-based motion correction algorithm, where cross-correlation among stripped OCT/OCTA images is used for motion estimation and correction [26]. A representative reconstruction pipeline is shown in Fig. 2. The OCTA image was calculated using a complex correlation mapping algorithm, as previously reported [28].

An OCTA image acquired in the ammonite coordinate system is shown on the leftmost side of Fig. 2, where the horizontal and vertical axes indicate the fast circle B-scan and slow spiral scan directions, respectively. First, rapid motions including micro-saccade were detected as a sudden change of the OCTA signal between adjacent fast scans, and the image was divided into multiple small strips. The maximum slow scan length of the strip was set to the number of pixels that corresponded to a data acquisition period of approximately 200 ms. Each strip was then remapped into Cartesian coordinates by considering the geometry of the circle scan position. As each strip was sufficiently short, no further lateral eye motion was estimated in the remapped image. One hand of the remapped strip was registered to the next remapped image by finding lateral motion which maximizes correlation between the remapped images. Then, they were merged together if the correlation exceeds a threshold and created a large field remapped image. By extending the registered area to a certain extent, this remapped image was regarded as the widefield OCTA image without noticeable lateral motions in the xy -plane. In this process, the strips with white horizontal lines due to eye motions were removed because of their low correlation with the registered image. The axial eye motions were then estimated and corrected to maximize the cross-correlation among the B-frame images in the cross-sectional plane by shift and tilt (skew) operations, so that the axial and transverse pixel length did not change. We assumed that the shift reflected axial eye motion for each B-frame and the tilt reflected OCT optical distortion due to change in alignment of OCT system relative to the measured eye during a measurement. Finally, a complete motion-corrected OCT and OCTA volume was obtained by remapping OCT and OCTA data according to the calculated lateral and axial motion. If there were more than two data points that were allocated to the same Cartesian coordinates after registration, they were averaged.

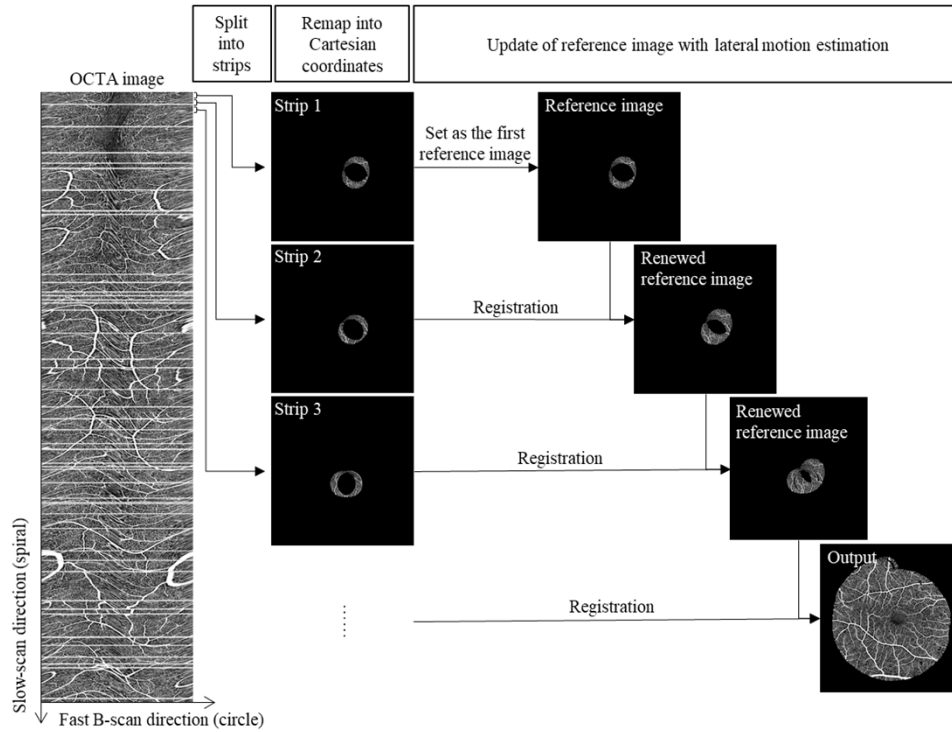


Fig. 2. Schematic of the reconstruction process for widefield OCTA. The OCTA SCP image captured in the ammonite coordinate was split into multiple strips and then remapped into Cartesian coordinates. Spatially overlapping strips in the Cartesian coordinate system were registered with each other, and this registered image formed the new reference image. This process continued until all the strips were merged together.

Topcon advanced boundary segmentation (TABS) software was used to perform layer segmentation in the OCT; subsequently, the *en-face* images could be extracted for any depth range. In this study, the superficial capillary plexus (SCP) was defined from the inner limiting membrane (ILM) to 20.8 μm below the boundary of the inner plexiform layer (IPL) and inner nuclear layers (INL). In addition, the deep capillary plexus (DCP) was defined from 20.8 μm below the IPL/INL to 67.6 μm below the IPL/INL, whereas the choriocapillaris (CC) layer was defined from the Bruch membrane (BM) to 10.4 μm below the BM. Further, an in-house projection artifact removal algorithm was applied when the *en-face* images were displayed.

2.4. VISTA process

In the original VISTA algorithm, a dimensionless metric for relative blood flow speed was calculated by taking the ratio of the OCTA signal at two different interscan times. The decorrelation (Decorr) defined by $(1 - \text{autocorrelation})$ was used as the OCTA signal. As the next generation VISTA, we adopted the quantitative blood flow speed marker recently proposed by Hwang *et al.* [29], where OCTA decorrelation signal intensities at different interscan times were fitted to a first-order saturation function given by Eq. (8). The model assumes that the temporal autocorrelation of the dynamic component of the OCT signal decays exponentially with a time constant τ , and the decorrelation reaches a saturation level D .

$$\text{Decorr}(t) = D \left\{ 1 - \exp \left(-\frac{t}{\tau} \right) \right\}. \quad (8)$$

In this study, an interscan time of 1.28 ms between 8 scan repetitions produced OCTA at seven different interscan times, from 1.28 ms to 8.96 ms. OCTA images with each interscan time were calculated by using all possible combinations. The OCTA images at different interscan times were reconstructed by using a same 3D displacement field determined through the method described in the previous section. For fitting, we used the reconstructed OCTA at six different interscan times, from 1.28 ms to 7.68 ms. The OCTA at 8.96 ms was not used owing to insufficient quality. The data points were weighted according to the number of averages to improve the accuracy of the time constant estimation. Here, the inverse of the calculated time constant ($1/\tau$) is defined as the flow parameter. A decorrelation signal lower than 0.05 was considered to indicate no flow. A false-colored OCTA image (hereinafter referred to as VISTA image) was then generated by superimposing the flow parameter onto the OCTA image [6]. The brightness of the VISTA image was determined from the averaged OCTA signal intensity within a slab along the depth direction and was mapped linearly from black to white. The VISTA image was color-mapped in a hue, saturation, and value color space, where the hue was linear to the flow parameter described above.

For a comparative study, conventional raster-scanning OCTA imaging was performed over an area of $3 \times 3 \text{ mm}^2$ (with 256×256 pixels) with the interscan time set to 1.44 ms. The number of repetitions was eight. The resulting measurement time was approximately 3.0 s.

2.5. Quantification of the VISTA images

Because blood flow velocity is assumed to be strongly dependent on vessel diameter [30], the vessel diameter must be considered when quantifying VISTA images and using them for diagnosis. Therefore, a series of image preprocessing steps was performed. First, the vessels in the OCTA image were enhanced using a Hessian filter and binarized by global/local thresholding [31]. Subsequently, the vessel image was skeletonized, and the center of the vessels was extracted. The vessel diameter was estimated from the byproduct of the Hessian filter, and the vessel diameter image was generated. In parallel, the VISTA image was generated through the process described in the previous section. Finally, the skeletonized vessel diameter and VISTA images were generated using the skeletonized vessel image as a mask. The same process was applied to the deep layer images. A comparison of the skeletonized vessel diameter and VISTA images allowed the quantification of flow parameters as a function of the vessel diameter. Note that by extracting the vessel center, the area-averaged flow parameter, for example, can be calculated without being affected by the vessel density. Through these procedures, the blood flow supply to the human retinal vasculature was analyzed objectively and statistically.

2.6. Subjects

Eyes of subjects were scanned using the proposed ammonite scan pattern, and the images were reconstructed using a previously described procedure. To evaluate the repeatability of the measurement, eight eyes of four normal subjects (age 25–37 years) were scanned in the study. All eyes were subjected to four repeated measurements within 1 h to reduce the effect of diurnal variation. This study was conducted at the Saga University Hospital, Japan. It was approved by the Institutional Review Board of Saga University and adhered to the tenets of the Declaration of Helsinki.

3. Results

3.1. Widefield VISTA imaging

Figure 3 shows the representative widefield OCT, OCTA, and VISTA images of a subject captured by the ammonite scan. In this case, the ammonite scan parameters were set to $L_f = 6.0 \text{ mm}$, $L_s = 102 \text{ mm}$, $L_\Delta = 1.1 \text{ mm}$, $N_f = 512$, and $N_s = 4096$. The number of repetitions was eight, and the interscan time was 1.28 ms. Figure 3(a) shows the wide-field

OCT projection image, and Fig. 3(b) shows the OCT B-scan images extracted from the yellow dotted line in Fig. 3(a). Figures 3 (c) and (d) show the OCTA and VISTA images of the SCP, respectively. High-resolution images were successfully obtained over the macular and optic disc regions without notable motion artifacts. The FOV was approximately 40° (~ 12 mm-diameter). The total acquisition time was 41.9 s. The widefield VISTA images visualize the large blood vessels as red (fast) and small blood vessels as green or blue (slow), as shown in Fig. 3(d).

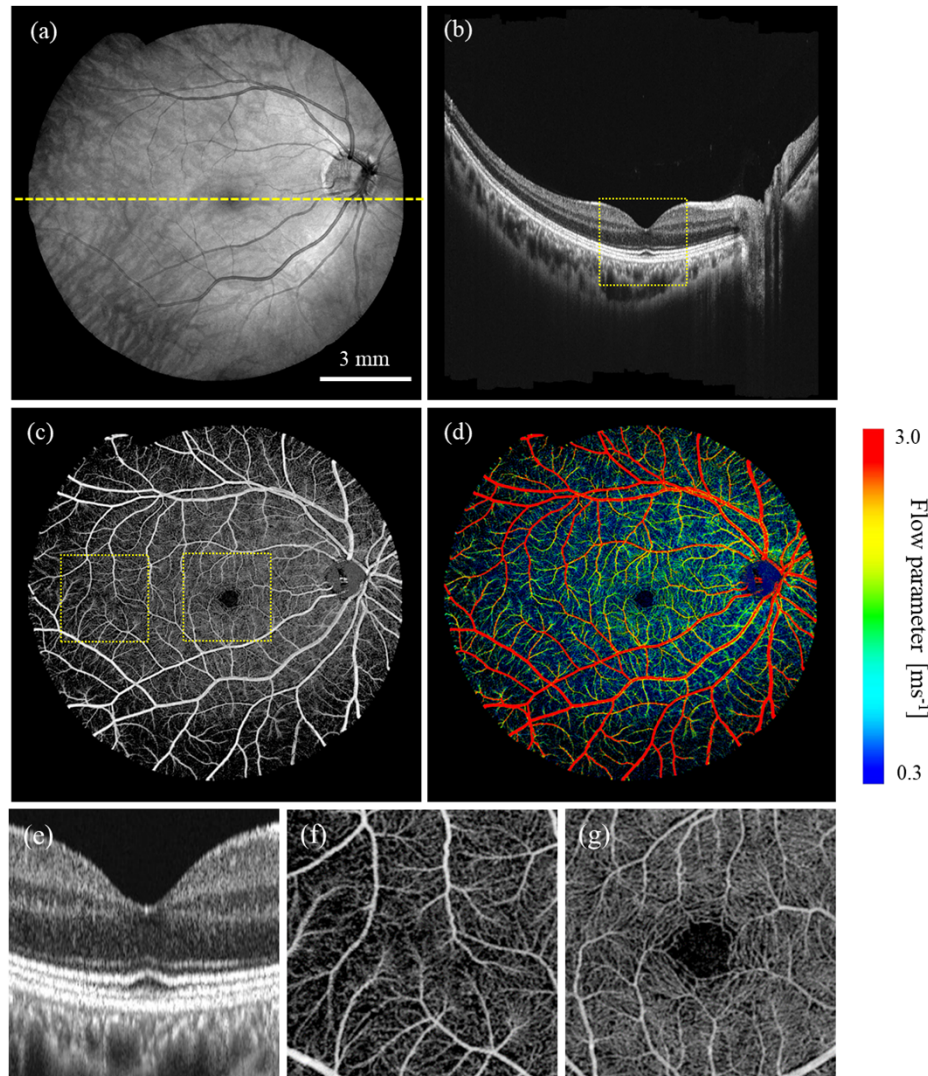


Fig. 3. Examples of the reconstructed ammonite-scanning OCT, OCTA, and VISTA images of a normal human eye. (a) Reconstructed OCT projection image. (b) Representative B-scan image extracted from the yellow line in (a). (c) OCTA image of SCP. (d) VISTA image of SCP. (e-g) Enlarged view of the B-scan and OCTA images shown in the yellow-rectangular location from (b) and (c). Size: 3×3 mm².

Figure 4 shows a comparison of ammonite-scanning and raster-scanning VISTA images of the same subject. Figures 4(a)-(c) show the VISTA images extracted from the widefield ammonite scan image shown in Fig. 3, and Figs. 4(d)-(f) show the VISTA images acquired by a conventional

raster scan. As described in Sec. 2.4, the interscan times were 1.28 and 1.44 ms for the ammonite and raster scans, respectively. A comparison of the images acquired with two different scan patterns yielded similar VISTA image appearances. This is because there is no significant difference in interscan time. The only notable difference is that ~ 3 horizontal strips possibly attributed to pulsation during the ~ 3 s data acquisition period were observed in the raster scan images in Figs. 4(d)-(f); however, they were averaged and suppressed in the ammonite scan images in Figs. 4(a)-(c).

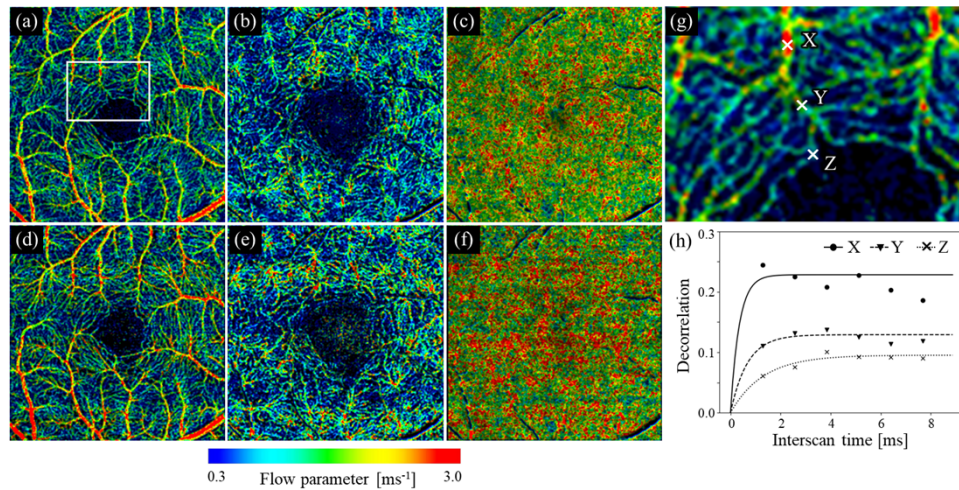


Fig. 4. Comparison of ammonite-scanning and raster-scanning VISTA images. (a)-(c) Ammonite scanning VISTA images of SCP, DCP, and CC, respectively, extracted from Fig. 3; (d)-(f) Corresponding VISTA images captured by a raster scan; (g) Enlarged view of the white square region in (a); (h) Time variation of the decorrelation signal at three representative points (X, Y, and Z) in (g) and their fitting results.

In the branching vascular network, the blood flow velocity decreased as it progressed to the end of the network. For example, the flow parameter at positions X, Y, and Z, indicated in Fig. 4(g), were determined by the exponential fitting for the interscan time-dependent OCTA decorrelation signal as shown in Fig. 4(h). The values were obtained as 2.87, 1.49, and 0.77 ms^{-1} , respectively. Further, the saturation levels of the decorrelation signal at positions X, Y, and Z were 0.24, 0.23, and 0.10, respectively.

3.2. Vessel diameter dependency of the flow parameter

As shown in Fig. 5(a), five small squares with a $2 \times 2 \text{ mm}^2$ area (center, nasal, superior, temporal, and inferior) were set as the regions of interest (ROIs) for the investigation, where the center ROI was aligned with the fovea center. Figures 5(b) and (c) show the average flow parameters measured for each ROI set on the SCP and DCP VISTA images. The results are plotted as a function of the estimated vessel diameter. The average flow parameter was strongly dependent on the vessel diameter and monotonically increased as the vessel diameter increased. A comparison of average flow parameters between SCP and DCP showed that the flow velocity in SCP was faster than that in DCP. In the normal eye, there were no remarkable differences or tendencies in the flow parameters with respect to the region being considered. See Supplement 1 for details on the VISTA images and corresponding vessel diameter images for each ROI.

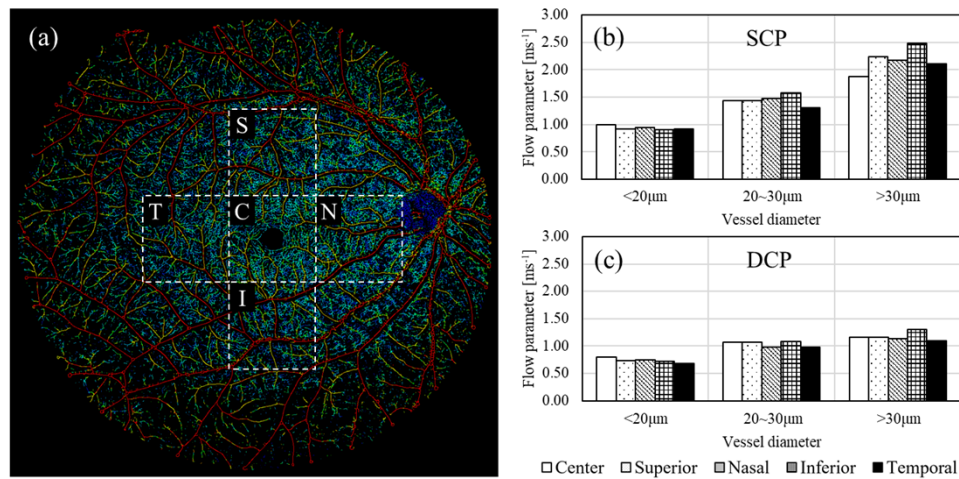


Fig. 5. Vessel diameter dependence of flow parameter in the (b) SCP and (c) DCP of a normal eye. In the analysis, the macula was divided into five square grid regions as shown in (a). C: center, N: nasal, S: superior, T: temporal, I: inferior.

3.3. Repeatability of flow parameter measurement

Figure 6 shows the measured flow parameters within a $3 \times 3 \text{ mm}^2$ area set on the macula center for eight eyes of four subjects. The average flow parameters across the subjects were $1.40 \pm 0.13 \text{ ms}^{-1}$ (SCP) and $1.06 \pm 0.13 \text{ ms}^{-1}$ (DCP) when only capillaries $\leq 30 \mu\text{m}$ in diameter were included. The average variability in the measurements indicated by error bars in the measurements was 0.05 ms^{-1} . It should be noted that the ratio of flow parameters between the SCP and DCP varied between 0.67 and 0.84 but seemed comparable between the left and right eyes. Capillary blood flow velocity in the SCP was significantly higher than that in the DCP ($p < 0.01$). A representative of four repeated measurements can be found in [Supplement 1](#).

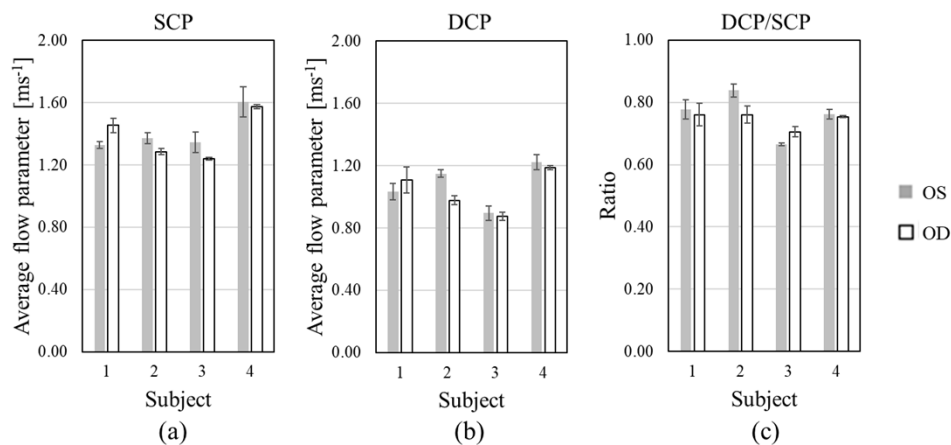


Fig. 6. Measured flow parameters in the (a) SCP, (b) DCP, and (c) their ratio. Error bars in the graphs indicate the standard deviation of each measurement repeated four times.

4. Discussion

Ammonite scanning VISTA allows the visualization of the spatial variations in blood flow in the widefield retina. The ammonite scan method enabled the extension of the FOV of VISTA imaging while maintaining a short interscan time. The interscan time in a point-scanning SS-OCT system was governed by the A-scan speed of the light source and the response speed of the fast-axis scanner. In this study, we achieved the dense sampling of 512 points along a 6-mm-long circle scan with an interscan time of 1.28 ms by driving a tunable VCSEL light source with an A-scan rate of 400 kHz and two axes of GSs with a scanning duty ratio close to 100%. The ammonite scan comprising small circle scans also offers the advantage of simultaneous driving of two axes of GSs during a fast scan, which improves the maximum scanning velocity by a factor of $\sqrt{2}$ compared with that of a raster scan. The A-scan rate of light sources may increase in the future, for example, with the advent of MHz-rate light sources [32], and the requirements for faster scanner response times will become more demanding. The proposed method would help in overcoming such challenging situations.

A wider FOV imaging system always requires lengthy measurement times, which inherently induces artifacts in eye motion. The motion-correction algorithm used for post-processing successfully produced VISTA images over the entire imaging area without notable motion artifacts, as shown in Figs. 2 and 3. For example, in Fig. 2, approximately 45 horizontal white lines could be observed on the original SCP image that was derived from eye movements during the imaging time. In our post-processing, these artifacts were successfully eliminated from the post-reconstruction image. Thus, the method is suitable for removing motion artifacts from eye movements, and widefield OCTA imaging is feasible without additional eye-tracking systems.

Flow measurement can be disrupted by a temporal alteration in blood flow and subject fluctuations, such as breezing, pulsation, and body motion. In the ammonite scan, the same location is scanned multiple times at different time points, and the blood flow alteration can be suppressed by temporal averaging. Hwang *et al.*, recently demonstrated the compensation of the fluctuation in the subject, as observed in Figs. 4(d)-(f) [29]. In the ammonite scan, we can apply the same processing prior to the reconstruction process and generate a fluctuation-compensated image in Cartesian coordinates.

The layer- and vessel-diameter-specific flow parameters were estimated as shown in Fig. 5. Such analysis is not possible with conventional dye-injection type testing including fluorescein angiography and indocyanine green angiography. Such analysis may facilitate highly sensitive detection of site-specific blood flow disorders.

Finally, the spatial averaging within ROIs sufficiently stabilized the measurement by suppressing the remaining local alteration in retinal blood flow. A sufficiently small inter-measurement variability, verified in Fig. 6, indicates the possibility of detecting blood flow impairment at a very early stage of vascular diseases and its alterations in the longitudinal data. The hypothesized capability of the present method for diseased eyes will be tested in future clinical studies.

Optimization of the interscan time may be necessary depending on the targeted pathology. In this study we have tried only interscan time of 1.28 ms with ammonite-scan method for measurements of healthy subjects in this study. However, VISTA with a longer interscan time was recently proposed for better visualization of blood flow in the low-velocity regime [33,34]. Although the optimal interscan time was determined based on the target velocity range of blood flow to be measured, the longer the interscan time, the more the number of motion artifacts tend to be introduced into the image. Consequently, a motion correction function and careful parameter optimization are needed for reliable measurement. Thus, the ammonite scan is considered to be suitable because it offers flexibility in terms of setting the scan parameters (interscan time, FOV, and sampling resolution) and a high tolerance against eye motions. Interestingly, when using techniques such as ammonite and Lissajous scans, a slight drift in the sample motion is considered preferable because it may improve the sampling density [26].

VISTA provides a quantitative surrogate parameter for blood flow velocity. However, the assumption of VISTA method that the flow parameter correlates with the blood flow velocity is a cause for concern along with several other uncertainties. Here, the scatterers in microvessels do not maintain their shape or flow in a simple constant motion [35]. In this regard, Lee *et al.* analyzed the origin of the decorrelation signal by dividing the “motion” into groups of static, flowing/diffusing, and entering/exiting [36]. Under this assumption, the authors separated the static, flowing, and diffusing components by fitting a few tens of acquired time points. However, using our approach, which had only seven measurement time points, the computation of such an analysis is challenging. In this study, therefore, the fitting process was simplified, and the flow parameter related to flow velocities was estimated without considering the type of motion. We are currently unable to extract detail information of motion (flowing/diffusing components and direction of flow); however, it is expected that a more quantitative analysis, as in the reference paper, can be realized by reducing the interscan time and increasing the number of scan repetitions.

In addition, there are remaining concerns regarding the size and anisotropy of the point spread function within the retina and the effects of projection artifacts. Although a more elaborate verification is required to explore the relationship between the measured flow parameters and absolute flow velocities, by taking the ratios of the flow parameters between different capillary layers or regions could eliminate the above uncertainties. Furthermore, it is important to understand the pathophysiology with an awareness of the layered structure of the capillaries in the retina. Retinal arterial blood spreads mainly from the superficial layer to the intermediate and deep layers. Compared to the superficial layer, a deep capillary network is more vulnerable to ischemic changes. For example, paracentral acute middle maculopathy is a blood flow disturbance in the intermediate layer, and acute macular neuroretinopathy is a blood flow disturbance in the deep layer [37]. The next step would be to perform an analysis based on the vessel segment [28], which would facilitate the interpretation and utilization of VISTA images by clinicians.

This paper mainly focuses on VISTA; however, we emphasize that the proposed method is also useful to widefield structural and standard OCTA imaging. The ammonite scan has a high affinity for the centrosymmetric shape of the eyeball. For example, dynamic adjustment of the positions of the OCT reference mirror and focusing optics to match the curvature of the fundus shape allows for proper measurement even with the limited image depth range of the OCT system. Although the imaging depth range and depth of focus in commercial OCT setups work for the FOV up to ~12 mm, this technique is useful to further extend the FOV in the future. Because our proposed method does not limit the circular trajectory, the optimal trajectory, such as an elliptical trajectory, can be selected according to the disease and application. The starting point of the initial measurement is not limited to the macula. The interest area can be scanned with varying sampling density depending on the retinal location.

Finally, the acquired data size increases with the FOV, redundancy of the scan, and number of repetitions. For example, the raw data size of the widefield ammonite scanning VISTA image demonstrated in Fig. 3 is approximately 95 GB. In this case, the reconstruction runtime for motion correction and merging was approximately 210 s, and the flow parameter calculation was 170 s in our environment. In addition, the data transfer time and general image processing (e.g., retinal layers segmentation) time are required before the final image output. Considering the efficient data handling in clinical settings, the total measurement time should be minimized to the best extent possible. In this regard, the ammonite scan combined with dynamic adjustment of the OCT reference mirror position is effective in reducing the size of the acquisition data. Onboard processing can also be a powerful solution to reduce computational costs during post-processing.

5. Conclusion

The relative blood flow velocity in the human retina was successfully visualized by combining ammonite scanning OCTA and VISTA with high spatial resolution without sacrificing the FOV and sampling density. The preliminary evaluation of relative blood flow velocity in healthy subjects reveals the velocity ratio in different layers with high repeatability. Precise and repeatable measurements of flow patterns across the retinal vascular network would provide crucial information for the early diagnosis and accurate prognosis of individual patients. In conclusion, the proposed ammonite scan may open new avenues for widefield OCT, OCTA, and VISTA imaging even with limited scanning speed, imaging depth range, and depth of focus; it can therefore increase the applicability of OCT devices in clinical settings. The proposed methods could be implemented in commercial OCT devices and utilized in routine clinical assessments.

Acknowledgments. We thank Dr. Eric M. Moulton, Dr. Jungeun Won (MIT), Mr. Stefan B. Ploner (FAU Erlangen-Nürnberg), and Dr. Nadia K. Waheed (Tufts Medical Center) for their fruitful discussions.

Disclosures. Provisional patent application No. 63/278,609. TM: Topcon (E), YM: Topcon (E), MT: Topcon (E), AM: Topcon (E), AK: Topcon (E), MA: Topcon (E), SM: Topcon (F), Yokogawa Electric (F), Nikon (F), Sky Technology (F), Kao (F), YY: Topcon (F), Yokogawa Electric (F), Nikon (F), Sky Technology (F), Kao (F), HE: Topcon (F), JGF: Optovue (I, P), Topcon (F), IP related to VISTA-OCTA (P)

Data availability. The data underlying the results presented in this paper are not publicly available at this time but may be obtained from the authors upon reasonable request.

Supplemental document. See [Supplement 1](#) for supporting content.

References

1. C. J. Pournaras, E. Rungger-Brändle, C. E. Riva, S. H. Hardarson, and E. Stefansson, "Regulation of retinal blood flow in health and disease," *Prog. Retinal Eye Res.* **27**(3), 284–330 (2008).
2. D.-Y. Yu, S. J. Cringle, P. K. Yu, C. Balaratnasingam, A. Mehnert, M. V. Sarunic, D. An, and E.-N. Su, "Retinal capillary perfusion: Spatial and temporal heterogeneity," *Prog. Retinal Eye Res.* **70**, 23–54 (2019).
3. R. F. Spaide, J. G. Fujimoto, N. K. Waheed, S. R. Sadda, and G. Staurengi, "Optical coherence tomography angiography," *Prog. Retinal Eye Res.* **64**, 1–55 (2018).
4. R. A. Leitgeb, "En face optical coherence tomography: a technology review [Invited]," *Biomed. Opt. Express* **10**(5), 2177 (2019).
5. D. M. Sampson, A. M. Dubis, F. K. Chen, R. J. Zawadzki, and D. D. Sampson, "Towards standardizing retinal optical coherence tomography angiography: a review," *Light: Sci. Appl.* **11**(1), 63 (2022).
6. S. B. Ploner, E. M. Moulton, W. Choi, N. K. Waheed, B. Lee, E. A. Novais, E. D. Cole, B. Potsaid, L. Husvagt, J. Schottenhamml, A. Maier, P. J. Rosenfeld, J. S. Duker, J. Horneegger, and J. G. Fujimoto, "Toward quantitative optical coherence tomography angiography: visualizing blood flow speeds in ocular pathology using variable interscan time analysis (VISTA)," *Retina* **36**(Supplement 1), S118–S126 (2016).
7. E. Moulton, W. Choi, N. K. Waheed, M. Adhi, B. K. Lee, C. D. Lu, V. Jayaraman, B. Potsaid, P. J. Rosenfeld, J. S. Duker, and J. G. Fujimoto, "Ultrahigh-speed swept-source OCT angiography in exudative AMD," *Ophthalmic Surgery Lasers and Imaging Retina* **45**(6), 496–505 (2014).
8. W. Choi, E. M. Moulton, N. K. Waheed, M. Adhi, B. Lee, C. D. Lu, T. E. De Carlo, V. Jayaraman, P. J. Rosenfeld, J. S. Duker, and J. G. Fujimoto, "Ultrahigh-speed, swept-source optical coherence tomography angiography in nonexudative age-related macular degeneration with geographic atrophy," *Ophthalmology* **122**(12), 2532–2544 (2015).
9. C. B. Rebhun, E. M. Moulton, E. A. Novais, C. Moreira-Neto, S. B. Ploner, R. N. Louzada, B. Lee, C. R. Bauman, J. G. Fujimoto, J. S. Duker, N. K. Waheed, and D. Ferrara, "Polypoidal choroidal vasculopathy on swept-source optical coherence tomography angiography with variable interscan time analysis," *Transl. Vis. Sci. Technol.* **6**, 1 (2017).
10. C. B. Rebhun, E. M. Moulton, S. B. Ploner, C. M. Neto, A. Y. Alibhai, J. Schottenhamml, B. Lee, W. Choi, F. A. Rifai, M. W. Tam, L. Husvagt, C. R. Bauman, A. J. Witkin, A. Maier, P. J. Rosenfeld, J. S. Duker, J. G. Fujimoto, and N. K. Waheed, "Analyzing relative blood flow speeds in choroidal neovascularization using variable interscan time analysis OCT angiography," *Ophthalmol. Retin.* **2**(4), 306–319 (2018).
11. E. M. Moulton, A. Y. Alibhai, C. Rebhun, B. Lee, S. Ploner, J. Schottenhamml, L. Husvagt, C. R. Bauman, A. J. Witkin, A. Maier, J. S. Duker, P. J. Rosenfeld, N. K. Waheed, and J. G. Fujimoto, "Spatial distribution of choriocapillaris impairment in eyes with choroidal neovascularization secondary to age-related macular degeneration: a quantitative OCT angiography study," *Retina* **40**(3), 428–445 (2020).
12. M. Arya, M. B. Filho, C. B. Rebhun, E. M. Moulton, B. Lee, Y. Alibhai, A. J. Witkin, C. R. Bauman, J. S. Duker, J. G. Fujimoto, and N. K. Waheed, "Analyzing relative flow speeds in diabetic retinopathy using variable interscan time analysis OCT angiography," *Ophthalmol. Retin.* **5**(1), 49–59 (2021).

13. P. S. Silva, J. D. Cavallerano, J. K. Sun, A. Z. Soliman, L. M. Aiello, and L. P. Aiello, "Peripheral lesions identified by mydriatic ultrawide field imaging: distribution and potential impact on diabetic retinopathy severity," *Ophthalmology* **120**(12), 2587–2595 (2013).
14. Q. Zhang, C. S. Lee, J. Chao, C.-L. Chen, T. Zhang, U. Sharma, A. Zhang, J. Liu, K. Rezaei, K. L. Pepple, R. Munsen, J. Kinyoun, M. Johnstone, R. N. V. Gelder, and R. K. Wang, "Wide-field optical coherence tomography based microangiography for retinal imaging," *Sci. Rep.* **6**(1), 22017 (2016).
15. F. P. Wang, S. S. Saraf, Q. Zhang, R. K. Wang, and K. A. Rezaei, "Ultra-widefield protocol enhances automated classification of diabetic retinopathy severity with optical coherence tomography angiography," *Ophthalmol. Retin.* **4**(4), 415–424 (2020).
16. V.-F. Duma, P. Tankam, J. Huang, J. Won, and J. P. Rolland, "Optimization of galvanometer scanning for optical coherence tomography," *Appl. Opt.* **54**(17), 5495 (2015).
17. E. M. Tang and Y. K. Tao, "Modeling and optimization of galvanometric point-scanning temporal dynamics," *Biomed. Opt. Express* **12**(11), 6701 (2021).
18. M. J. Ju, M. Heisler, A. Athwal, M. V. Sarunic, and Y. Jian, "Effective bidirectional scanning pattern for optical coherence tomography angiography," *Biomed. Opt. Express* **9**(5), 2336 (2018).
19. X. Wei, T. T. Hormel, S. Pi, Y. Guo, Y. Jian, and Y. Jia, "High dynamic range optical coherence tomography angiography (HDR-OCTA)," *Biomed. Opt. Express* **10**(7), 3560 (2019).
20. O. M. Carrasco-Zevallos, C. Viehland, B. Keller, R. P. McNabb, A. N. Kuo, and J. A. Izatt, "Constant linear velocity spiral scanning for near video rate 4D OCT ophthalmic and surgical imaging with isotropic transverse sampling," *Biomed. Opt. Express* **9**(10), 5052 (2018).
21. S. Ni, T.-T. P. Nguyen, R. Ng, S. Khan, S. Ostmo, Y. Jia, M. F. Chiang, D. Huang, J. P. Campbell, and Y. Jian, "105° field of view non-contact handheld swept-source optical coherence tomography," *Opt. Lett.* **46**(23), 5878 (2021).
22. K. Liang, Z. Wang, O. O. Ahsen, H.-C. Lee, B. M. Potsaid, V. Jayaraman, A. Cable, H. Mashimo, X. Li, and J. G. Fujimoto, "Cycloid scanning for wide field optical coherence tomography endomicroscopy and angiography in vivo," *Optica* **5**(1), 36–43 (2018).
23. Y. Chen, Y.-J. Hong, S. Makita, and Y. Yasuno, "Three-dimensional eye motion correction by Lissajous scan optical coherence tomography," *Biomed. Opt. Express* **8**(3), 1783 (2017).
24. Y. Chen, Y.-J. Hong, S. Makita, and Y. Yasuno, "Eye-motion-corrected optical coherence tomography angiography using Lissajous scanning," *Biomed. Opt. Express* **9**(3), 1111 (2018).
25. S. Makita, M. Miura, S. Azuma, T. Mino, T. Yamaguchi, and Y. Yasuno, "Accurately motion-corrected Lissajous OCT with multi-type image registration," *Biomed. Opt. Express* **12**(1), 637 (2021).
26. S. Makita, S. Azuma, T. Mino, T. Yamaguchi, M. Miura, and Y. Yasuno, "Extending field-of-view of retinal imaging by optical coherence tomography using convolutional Lissajous and slow scan patterns," *Biomed. Opt. Express* **13**(10), 5212 (2022).
27. M. Tamura, Y. Moriguchi, S.-Y. Yeh, A. Matsumoto, M. Shibutani, T. Asao, T. Mino, M. Nakanishi, A. Kubota, and M. Akiba, "Sensorless astigmatism correction using a variable cross-cylinder for high lateral resolution optical coherence tomography in a human retina," *Appl. Opt.* **60**(30), 9553 (2021).
28. S. Makita, K. Kurokawa, Y.-J. Hong, M. Miura, and Y. Yasuno, "Noise-immune complex correlation for optical coherence angiography based on standard and Jones matrix optical coherence tomography," *Biomed. Opt. Express* **7**(4), 1525 (2016).
29. Y. Hwang, J. Won, A. Yaghy, H. Takahashi, J. M. Girgis, K. Lam, S. Chen, E. M. Moul, S. B. Ploner, A. Maier, N. K. Waheed, and J. G. Fujimoto, "Retinal blood flow speed quantification at the capillary level using temporal autocorrelation fitting OCTA," *arXiv*, arXiv:2302.11612 (2023).
30. G. Garhofer, R. Werkmeister, N. Dragostinoff, and L. Schmetterer, "Retinal blood flow in healthy young subjects," *Invest. Ophthalmol. Visual Sci.* **53**(2), 698–703 (2012).
31. R. Reif, J. Qin, L. An, Z. Zhi, S. Dziennis, and R. Wang, "Quantifying optical microangiography images obtained from a spectral domain optical coherence tomography system," *Int. J. Biomed. Imaging* **2012**, 509783 (2012).
32. T. Klein and R. Huber, "High-speed OCT light sources and systems [Invited]," *Biomed. Opt. Express* **8**(2), 828 (2017).
33. Y. Kaizu, S. Nakao, T. Soda, J. Horie, I. Wada, M. Yamaguchi, A. Takeda, and K. Sonoda, "Longer interscan times in OCT angiography detect slower capillary flow in diabetic retinopathy," *Ophthalmology Science* **2**(3), 100181 (2022).
34. N. Nishigori, Y. Muraoka, M. Ishikura, S. Kadomoto, Y. Mori, S. Numa, T. Murakami, S. Ooto, and A. Tsujikawa, "Macular blood flow changes in branch retinal vein occlusion examined by optical coherence tomography angiography variable interscan time analysis," *Retina* **42**(11), 2210–2217 (2022).
35. P. Bedggood and A. Metha, "Direct visualization and characterization of erythrocyte flow in human retinal capillaries," *Biomed. Opt. Express* **3**(12), 3264 (2012).
36. J. Lee, W. Wu, J. Y. Jiang, B. Zhu, and D. A. Boas, "Dynamic light scattering optical coherence tomography," *Opt. Express* **20**(20), 22262 (2012).
37. D. Sarraf, E. Rahimy, A. A. Fawzi, E. Sohn, I. Barbazetto, D. N. Zacks, R. A. Mitra, J. M. Klancnik, S. Mrejen, N. R. Goldberg, R. Beardsley, J. A. Sorenson, and K. Bailey Freund, "Paracentral acute middle maculopathy a new variant of acute macular neuroretinopathy associated with retinal capillary ischemia," *JAMA Ophthalmol.* **131**(10), 1275–1287 (2013).